



HAL
open science

Extremely thin crust in the Indian Ocean possibly resulting from Plume–Ridge Interaction

Satish C. Singh, H el ene Carton, Ajay. S. Chauhan, Sophie Androvandi, Anne Davaille, J er ome Dymont, Mathilde Cannat, Nugroho. D. Hananto

► To cite this version:

Satish C. Singh, H el ene Carton, Ajay. S. Chauhan, Sophie Androvandi, Anne Davaille, et al.. Extremely thin crust in the Indian Ocean possibly resulting from Plume–Ridge Interaction. *Geophysical Journal International*, 2010, 184 (1), pp.29-42. <10.1111/j.1365-246X.2010.04823.x>. <insu-01309448>

HAL Id: insu-01309448

<https://insu.hal.science/insu-01309448v1>

Submitted on 29 Apr 2016

HAL is a multi-disciplinary open access archive for the deposit and dissemination of scientific research documents, whether they are published or not. The documents may come from teaching and research institutions in France or abroad, or from public or private research centers.

L'archive ouverte pluridisciplinaire **HAL**, est destin ee au d ep ot et  a la diffusion de documents scientifiques de niveau recherche, publi es ou non,  emanant des  tablissements d'enseignement et de recherche fran ais ou  trangers, des laboratoires publics ou priv es.



HAL Authorization

Extremely thin crust in the Indian Ocean possibly resulting from Plume–Ridge Interaction

Satish C. Singh,¹ H el ene Carton,¹ Ajay S. Chauhan,¹ Sophie Androvandi,² Anne Davaille,³ J er ome Dymont,¹ Mathilde Cannat¹ and Nugroho D. Hananto¹

¹Laboratoire de G eosciences Marines, Institut de Physique du Globe de Paris – CNRS, 1 rue Jussieu, 75238 Paris Cedex 05, France.

E-mail: singh@ipgp.jussieu.fr

²Laboratoire de Dynamique des Fluides G eologiques, Institut de Physique du Globe de Paris – CNRS, 1 rue Jussieu Jussieu, 75238 Paris Cedex 05, France

³Laboratoire FAST (CNRS/U-Psud/UPMC), Bat. 502, Rue du Belv ed ere, Campus Universitaire, 91405 ORSAY cedex, France

Accepted 2010 September 24. Received 2010 September 21; in original form 2009 December 25

SUMMARY

The thickness of the crust created at ocean spreading centres depends on the spreading rate and melt production in the mantle. It is ~5–8 km for a crust formed at slow and fast spreading centres and 2–4 km at ultra-slow spreading centres away from hotspots and mantle anomalies. The crust is generally thin at the fracture zones and thick beneath hotspots and large igneous provinces. Here we present results for the crust generated at the fast Wharton spreading centre 55–58 Ma ago using seismic reflection and refraction data. We find that the crust over a 200 km segment of the Wharton Basin is only 3.5–4.5 km thick, the thinnest crust ever observed in a fast spreading environment. A thin crust could be produced by the presence of depleted and/or cold mantle. Numerical simulations and recent laboratory experiments studying the impact of a hot plume under a lithosphere show that a curtain of weak cold downwellings of depleted mantle material is likely to develop around the edges of the hot plume pond. Because of a strongly temperature-dependent viscosity of lithospheric material, the hotter, therefore less viscous, bottom of the lithosphere can be mobilized by an impinging plume. If sampled by a spreading centre, the locally cold and depleted mantle should result in low production of melt. We suggest that the observed thin crust in the Wharton Basin is likely to have been formed by the interaction between the Kerguelen mantle plume and the Wharton spreading centre ~55 Ma ago.

Key words: Mantle processes; Hotspots; Crustal structure; Indian Ocean.

1 INTRODUCTION

Over 70 per cent of the Earth's crust is formed at ocean spreading centres, and therefore it is fundamental to understand how this crust is formed in different environments. The thickness of the oceanic crust provides an indication of geodynamics condition during the crustal formation. Most of our knowledge of the oceanic crustal thickness is based on seismic reflection and refraction experiments in different settings, such as spreading centres, fracture zones, large oceanic igneous provinces, continental margins and subduction zones (Reid & Jackson 1981; Chen 1992; White *et al.* 1992; Bown & White 1994). The crust formed at fast spreading centres away from hotspots and mantle anomalies is generally uniform and 6–7 km thick (White *et al.* 1992; Eittreim *et al.* 1994) but some variations (6–8 km) have been observed recently (Barth & Mutter 1996; Canales *et al.* 2002; Singh *et al.* 2006). There is no significant crustal thickness variation across fracture zones in fast spreading environment, where it is also 5.5–6 km thick (van Avendonk *et al.* 2001). The crust formed at slow spreading centres is generally thick

at the centre of the segment (6–7 km) and thin at segment ends (Barclay *et al.* 1998). The fracture zones in slow spreading environment are generally thin (3–4.5 km) (Detrick *et al.* 1993). The thinnest crust is formed at ultra-slow spreading centres (Mueller *et al.* 2000; Jokat & Schmidt-Aursch 2007). These observations suggest that the thickness of the crust depends on the spreading rate and melt supply to the crust. On the other hand, thicker crust is found beneath large igneous provinces, along hotspot tracks or at the intersection of plume and ridges, and is believed to be formed by higher mantle temperatures due to the presence of a plume (e.g. Parkin & White 2008). The presence of a plume around a spreading centre would have a significant effect on the crustal thickness variation, and we show here that a plume might also help to create a thin crust as well.

Although the crust formed at fast spreading centres are usually 6 km thick, thinner crust has been observed at some places. For example, 5-km-thick crusts were observed near the South American trench (Grevemeyer *et al.* 2007) and IODP Hole 1256 (Hallenborg *et al.* 2003) that were formed at the EPR 20–24 Ma and 17–20 Ma

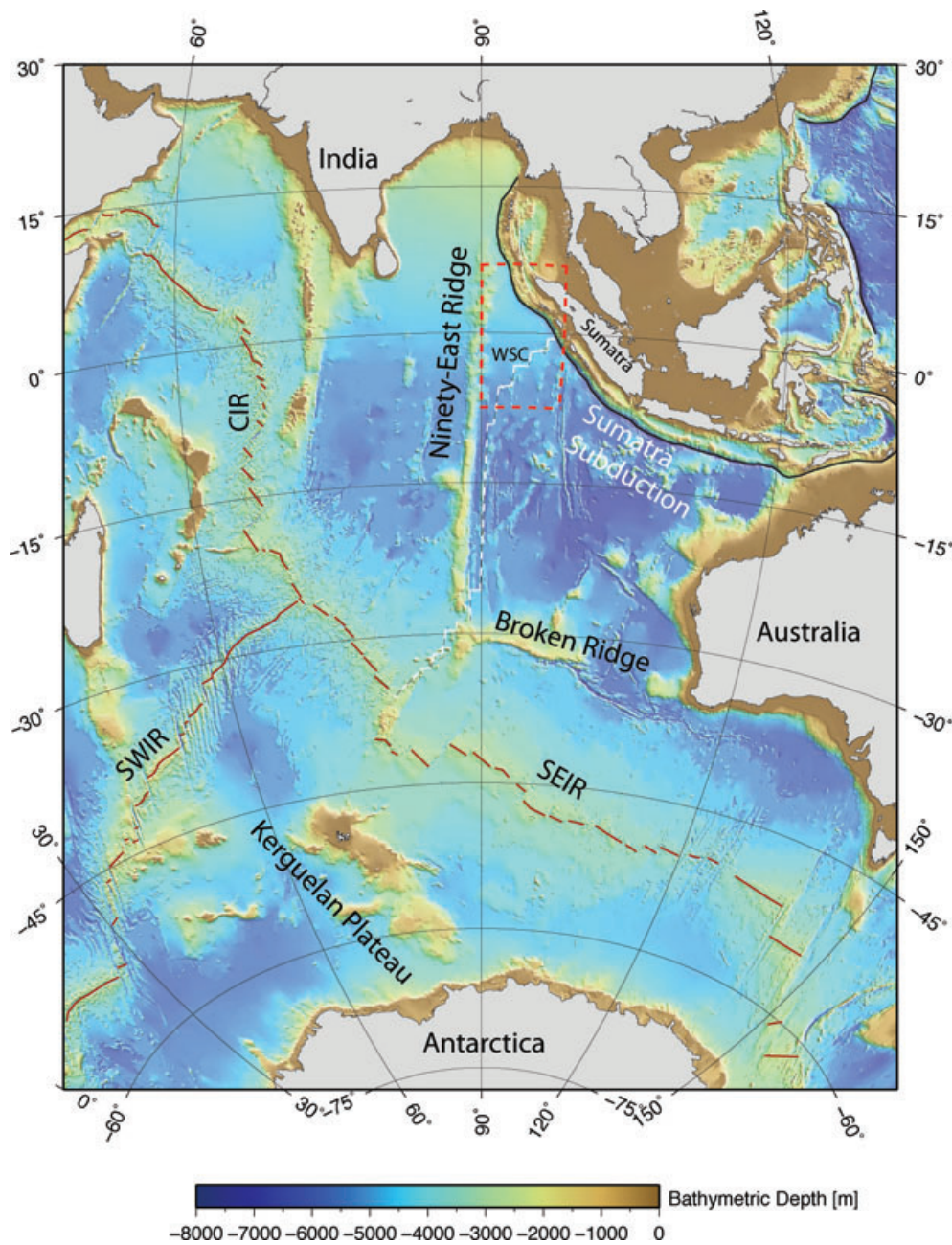


Figure 1. Bathymetric map showing important tectonic features. WSC, Fossil Wharton Spreading Centre; SEIR, South East Indian Ridge; SWIR, Southwest Indian Ridge; CIR, Central Indian Ridge. Ridges are marked by red curves and subduction zone by black. White lines indicate the position of fossil WSC. Dashed rectangle marks area shown in Fig. 2.

ago, respectively. Here we present results from the Wharton Basin in the Indian Ocean where we find a very thin crust (3.5–4.5 km). Using a recent analogue modelling study we suggest that the thin crust could be produced by the interaction between the Wharton spreading centre and the nearby Kerguelen hot mantle plume 55–58 Ma ago.

2 WHARTON BASIN

The Wharton Basin lies east of the Ninety-East Ridge, which is one of most impressive bathymetric feature in the Indian Ocean. The crust in the Indian Ocean is formed at three active spreading cen-

tres, namely Central Indian Ridge (CIR), Southwest Indian Ridge (SWIR), Southeast Indian Ridge (SEIR) and the fossil Wharton Spreading Centre (WSC) (Fig. 1). The SEIR separates the Indo-Australian Plate from the Antarctica Plate, each of which contains conjugate continental blocks of Broken Ridge and Kerguelan Plateau, respectively.

The crust in the Wharton Basin was formed at the WSC from 133 to 40 Ma. Seafloor spreading in the Wharton Basin initiated around 133 Ma (magnetic anomaly M10) at the WSC, separating India from Australia (Liu *et al.* 1983; Fullerton *et al.* 1989). Probably during the same time, the spreading initiated at the Southeast Indian Ridge (SEIR) separating Antarctica from India (Gaina *et al.* 2007). The large igneous province of the Kerguelen Plateau and the Broken

Ridge was mostly formed between 119 and 95 Ma (Frey *et al.* 2003). At ~ 96 Ma Australia and Antarctica started to break apart (Tikku & Cande 1999), and the spreading direction changed from NW–SE to N–S on both the SEIR and the WSC (Liu *et al.* 1983; Fullerton *et al.* 1989). The spreading rate at the WSC progressively increased from a full rate of 40 mm yr^{-1} at 80 Ma to 150 mm yr^{-1} at 67 Ma as India started to move rapidly northwards, then slowed down at 50 Ma, reaching 50 mm yr^{-1} at 45 Ma (Royer & Sandwell 1989) when India collided with Eurasia. Similarly, the spreading rate at SEIR increased from 90 to 210 mm yr^{-1} and then slowed down to 100 mm yr^{-1} during the same time span. During this period, the fast northward motion of the Indian Plate over the Kerguelen plume tail resulted in the creation of the Ninety-East Ridge (Sclater & Fisher 1974; Royer & Sandwell 1989). The nearby spreading centres remained strongly influenced by the plume. The SEIR developed a strong asymmetry through successive ridge jumps to remain in the vicinity of the Kerguelen plume (Royer & Sandwell 1989). As a consequence, the large fracture zones located east of the Ninety-East Ridge grew even longer and the main part of the WSC (now located east of 91°E) became disconnected from the plume head. Spreading at the WSC ceased around 40 Ma (Liu *et al.* 1983), when the Indian Ocean spreading centres went through a major reorganization as a consequence of India's hard collision with Eurasia (Patriat & Achache 1984). A significant part the Wharton Basin lithosphere has subducted beneath the Sumatra subduction zone.

Using seafloor bathymetry and shallow seismic reflection data, Deplus *et al.* (1998) suggested that the western Wharton Basin is deforming where the movement is taking place along re-activated fracture zones. The presence of left-lateral strike-slip earthquakes in the region further confirms this observation (Abercrombie *et al.* 2003; Engdahl *et al.* 2007). A recent bathymetry study near the subduction front shows similar deformation (Graindorge *et al.* 2008).

Our study area lies at the northern part of the Wharton Basin near the Sumatra subduction front (Fig. 2), where the crust is formed between magnetic anomalies 23 and 26 (52–58 Ma), east of Ninety-East Ridge. The fossil Wharton Spreading ridge subducts beneath the Sumatra near 97°E . There are about eight fracture zones between this and the Ninety-East Ridge, four of (F4–F7) which lie within our study area (Fig. 2).

3 SEISMIC REFLECTION DATA

As a part of the Great Sumatra earthquake study, a 233-km-long trench parallel deep seismic reflection profile was shot on board the WesternGeco M/V Geco Searcher in July 2006. The profile, called WG3, runs between 32 and 66 km from the subduction front. The spreading direction was N–S, profile WG3 is about $\text{N}50^\circ\text{S}$ and hence traverses over a 55- to 58-Ma-old oceanic crust (Liu *et al.* 1993) (Fig. 2), and cuts the two fracture zones (F5 and F6). Two dip lines (WG1 and WG2) were shot traversing the subduction system orthogonally, crossing the subduction front, accretionary prism, fore-arc basin and volcanic arc (Singh *et al.* 2008; Chauhan *et al.* 2009). Here, we shall mainly focus on the oceanic part of these lines.

One 12 km and another 5.5 km long Q-Marine streamers were deployed at 15 and 7.5 m water depth to enhance low-frequency energy on the deeper streamer and high-frequency energy on the shallower. The vertical and lateral positions of the streamer were controlled by compass birds and Q-Fins streamer steering devices placed at ~ 300 m intervals. Surface buoys with GPS antennae were placed both at the beginning and at the end of the streamers. The precise locations of the first 5.5 km of the streamers were deter-

mined in real time using acoustic transponders also placed every 300 m. A large airgun array comprising six subarrays (48 tuned airguns totalling $10\,170 \text{ in}^3$) was used as a source, and provided 330-bar-m output. The airgun array was towed at a 15 m depth and fired at 50 m intervals. The Q-Marine streamer contains hydrophones at 3.125 m intervals, which were digitized and low-cut filtered (2 Hz). The digital signals were then spatially resampled to a 12.5 m receiver interval after applying digital noise attenuation techniques and appropriate digital spatial anti-alias filter providing 958 channels (Martin *et al.* 2000). The sampling interval was 2 ms and the record length was 20.48 s. The vessel speed varied from 4.2 to 4.8 knots.

Because we were interested in deep structure, the data was re-sampled to 8 ms and filtered using a zero-phase 52.5 Hz 60 dB/oct anti-alias filter. The swell noise was removed using three passes of swell noise attenuation technique in frequency ranges 0–10, 10–62.5 and 0–20 Hz. A time varying beam-forming filter for a Fresnel radius corresponding to 12 Hz was applied first in the shot domain and then in the receiver domain to reduce scattering noise. A semblance velocity analysis was carried out every 2 km along the profile. The data were NMO corrected and stacked after appropriate mute. After stacking, the migration was subsequently performed using a 2-D Kirchhoff algorithm and a smooth velocity model obtained during stacking. Depth conversion of the migrated image was performed using a velocity model determined after stacking.

4 SEISMIC REFLECTION RESULTS

Seismic reflection image along profile WG3 as a function of two-way traveltimes is shown in Fig. 3(a) and the depth converted image using interval velocity obtained from normal moveout velocity in Fig. 3(b). The water depth varies from 4.7 km in the southeast to 4.4 km in the northwest. There are thick (2–2.5 s) turbiditic sediments over a strong negative polarity at ~ 200 ms above the basement, which Dean *et al.* (2010) interpret to be due to a pre-decollement surface (seaward propagation of the megathrust). On profile WG3, which is at about 60 km from the subduction front, this reflector also has a negative polarity and is present along the most part of the profile, interrupted by basement highs. It is also present along the oceanic part of profile WG1 (Singh *et al.* 2008, Fig. 4) for about 60 km from the subduction and shows the similar behaviour. There are other reflectors in the sedimentary column that have negative polarity, and therefore, we think that the negative polarity reflection of Dean *et al.* is a lithological boundary in the sediments as it is very wide-spread and interrupted by the basement highs. Singh *et al.* (2008) interpret this reflector to be the top of the pelagic sediments, which seems to be present over the oceanic crust along most of the Andaman–Sumatra margin.

The basement, top of the oceanic crust, is well imaged. The lower sediments show sign of some folding and faulting. Near fracture zone F5, a flower structure in the sediments and a low basement relief is observed, suggesting the presence of strike-slip motion. Although no magnetic anomalies associated with fracture zones F6 and F7 are observed along profile WG3, the northward extrapolation of fracture zone F6 crosses profile WG3 and coincides with a basement high/ridge (500 ms) and has a 30 m vertical offset on the seafloor. There is a significant basement relief NW of F6, suggesting the region between F6 and F7 is complex as indicated by magnetic anomaly study (Fig. 2). There seems to be several normal faults in this region, some of them continue from seafloor down to the basement. They could be interpreted to be either due to normal

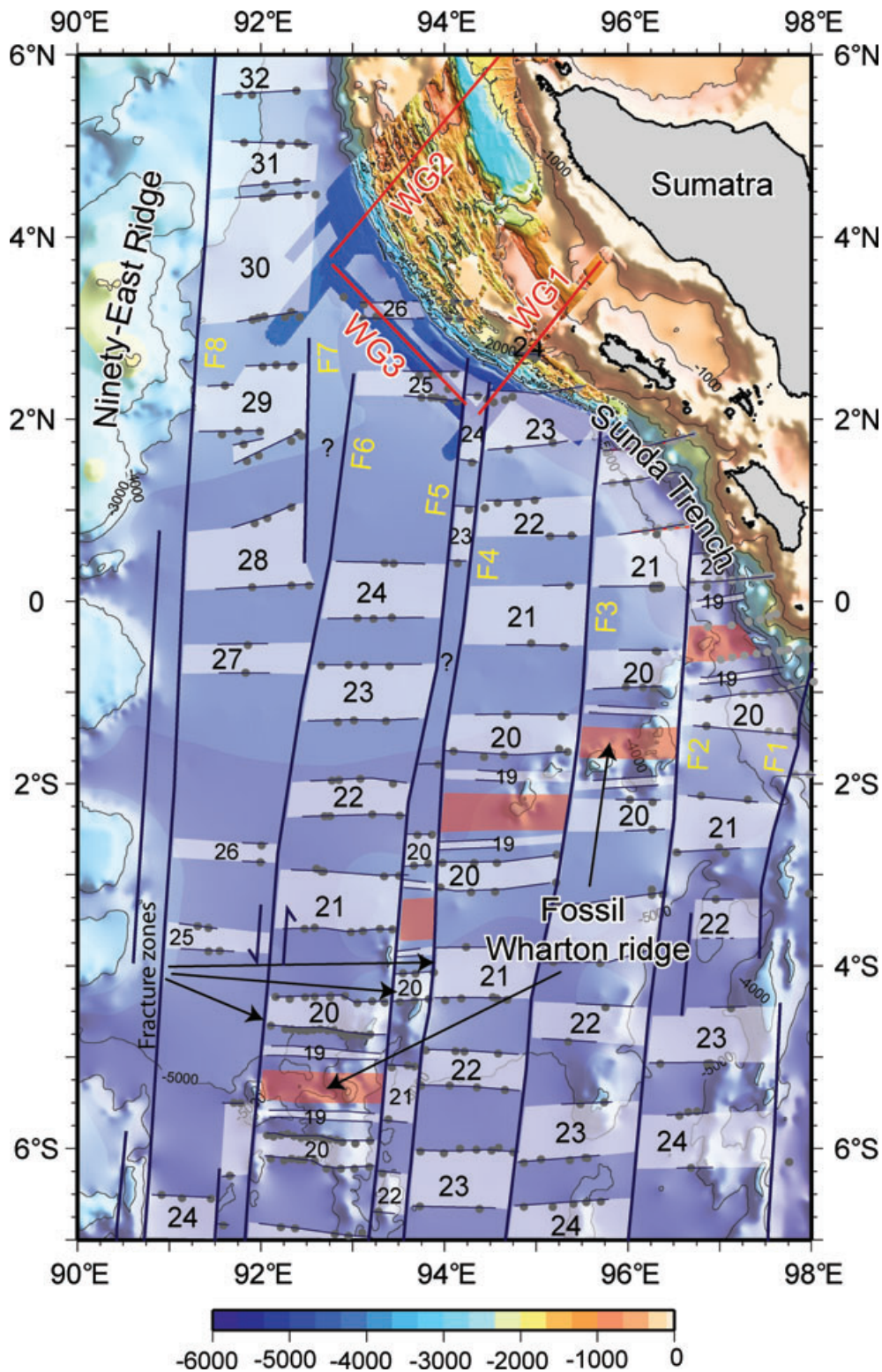


Figure 2. Seafloor bathymetry and magnetic anomalies in the eastern Indian Ocean. The magnetic anomalies were reconstructed from all existing and recently acquired data (black dots). The Ninety-East ridge is clearly visible as a N–S bathymetric high. The fossil spreading centre (Wharton ridge) is marked in light red, fracture zones (N5°E azimuth) identified from altimetry data are marked with navy blue lines (F1–F8), and seismic profiles with red lines. Fracture zones F5 and F6 intersect seismic profile WG3. Profile WG3 is 233 km long, 32–66 km from the Sumatra subduction front and cuts the fracture zones at ~49° angle. Magnetic anomalies are marked by anomaly numbers and white stripes, and anomalies versus age relationships are as follows: 32 = 72 Ma, 31 = 68 Ma, 30 = 67 Ma, 29 = 65 Ma, 28 = 63 Ma, 27 = 61 Ma, 26 = 58 Ma, 25 = 56 Ma, 24 = 53 Ma, 23 = 52 Ma, 22 = 49 Ma, 21 = 47 Ma, 20 = 43 Ma, 19 = 41 Ma. Colour scale represents bathymetry in metres.

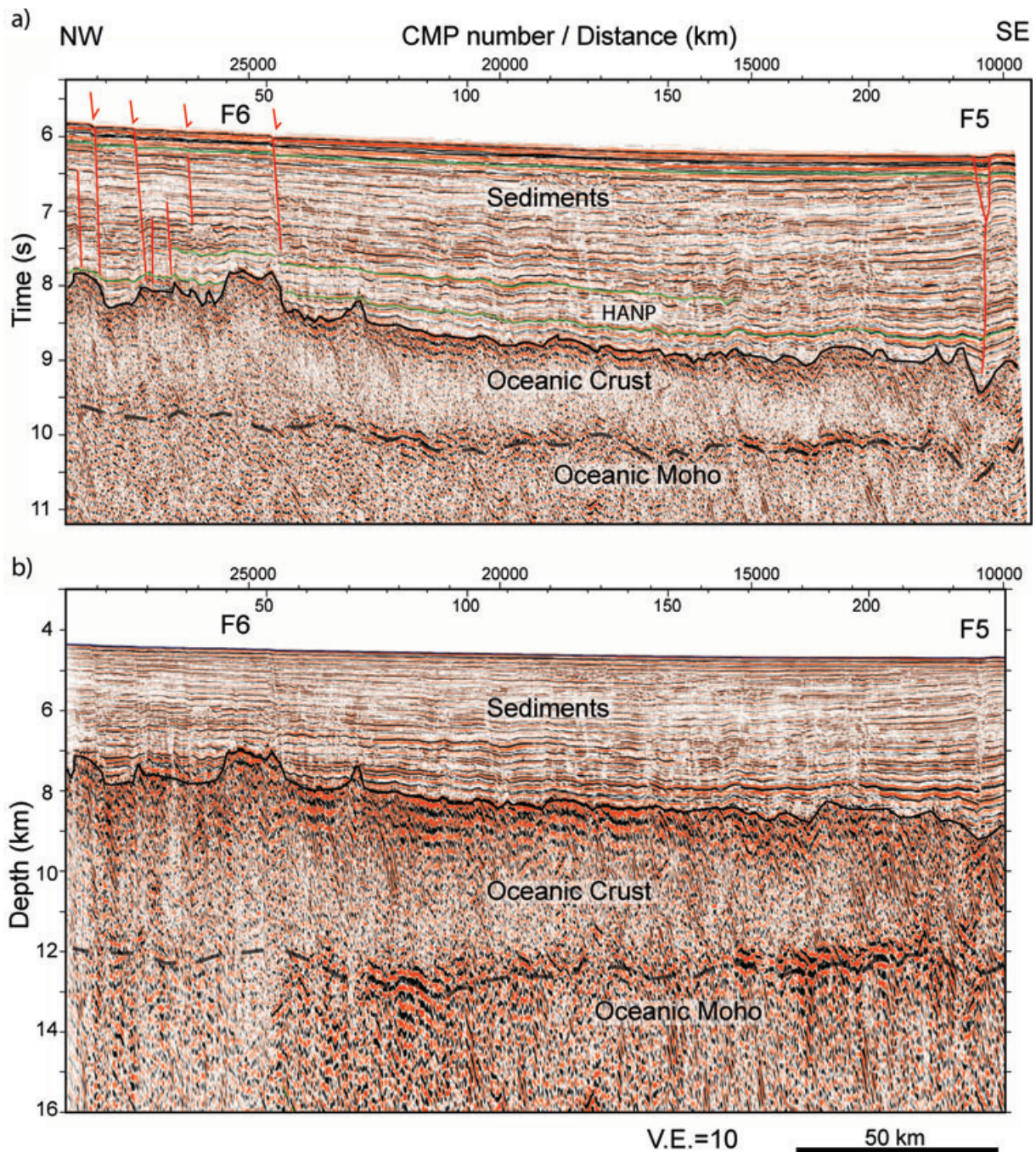


Figure 3. (a) Interpreted seismic reflection image along WG3 profile in time. Vertical to horizontal scale = 10:1 for a velocity of 1.5 km s^{-1} . F5 and F6 are the two fracture zones crossing the profile. Green curves highlight the sedimentary strata with clear negative polarity, thin black curve the basement and thick black dashed the Moho. HANP is the high amplitude negative polarity reflector pointed out by Dean *et al.* (2010). The crustal thickness varies from 1.1 s in the SE to 1.45 s in the NW. Red lines represent faults. (b) Depth converted image without much interpretation.

faulting related to plate bending or dip-slip along the strike-slip faults. However, the absence of any significant normal faulting SE of F6 suggests that the vertical offsets observed between F6 and F7 should be associated with dip-slip motion along the strike-slip faulting between F6 and F7.

There is a strong continuous reflector at 1.1–1.4 s two-way traveltimes (3.5–4.5 km) below the basement that can be followed for about 200 km along the profile (Fig. 3). The dominant frequency of the reflection is low (10–20 Hz), suggesting that it is not due to

out-of-plane reflections from the seafloor and sedimentary strata, but from deep crust. This reflector is too deep to be a reflection from the gabbro-dyke boundary and seems shallow if it is a reflection from the crust–mantle boundary (Moho) for a crust formed at a fast spreading centre. The gabbro-dyke boundary, which is a proxy for axial magma chamber depth, is at ~ 1 –2 km below the seafloor at fast spreading centres (Detrick *et al.* 1987; Singh *et al.* 1998) and has been some times imaged beneath old crusts as weak reflections (Ranero *et al.* 1997; Hallenberg *et al.* 2003). There are many

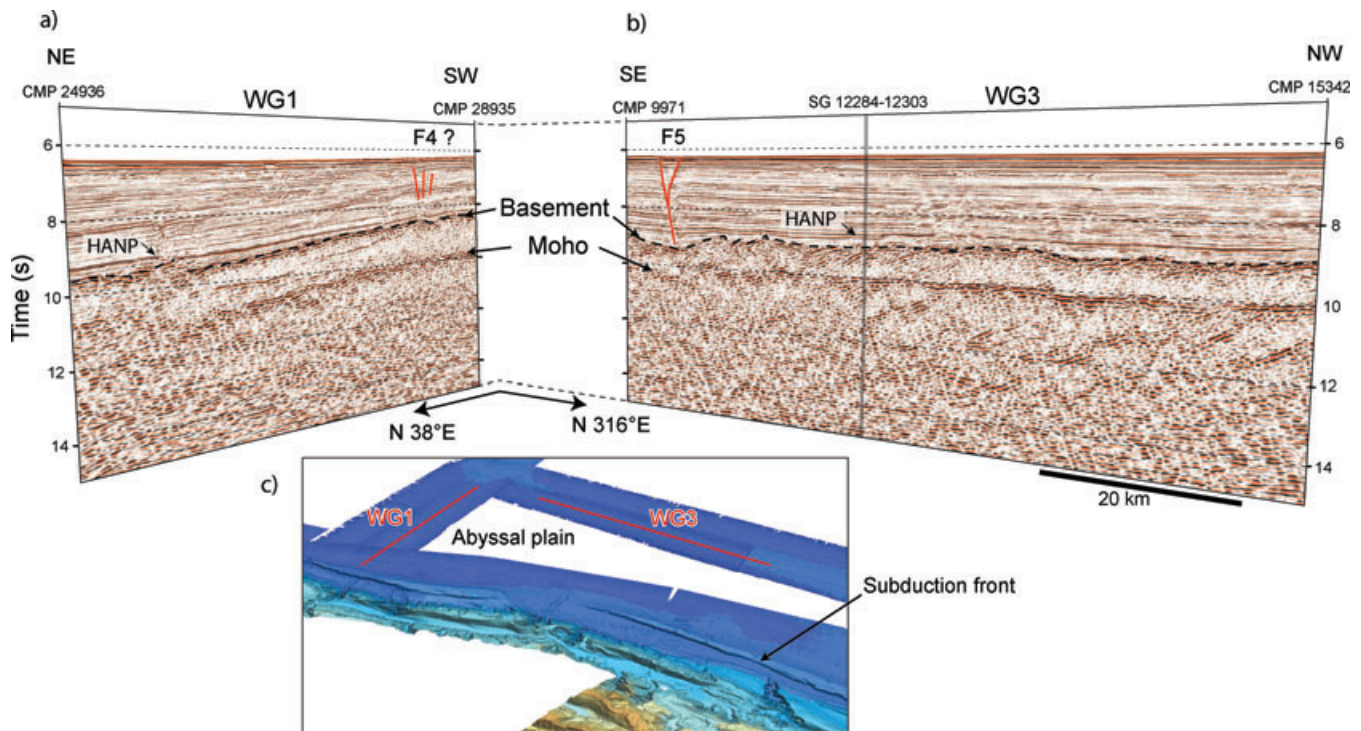


Figure 4. Fence diagram of sediments and Moho on lines WG1 (dip line) (a) and WG3 (trench parallel line) (b) presented as time sections. The location of the CDP used in Fig. 5. Vertical to horizontal scale = 4:1 at the seafloor. The orientations and positions of the lines are shown in the bathymetric image below (c). The view is from the subduction front towards the Indian Ocean. The sediments thicken and the plate bends towards the trench on profile WG1. The crust is ~ 1.1 s thick on WG3 and ~ 1.4 s on WG1. F4 and F5 are the fracture zones. The dipping reflections on profile WG3 are mantle reflections that have been imaged down to 35 km depth (Singh *et al.* 2007). HANP, high amplitude negative polarity reflector (Dean *et al.* 2010).

dipping reflections imaged below this reflector down to 35 km depth (Singh *et al.* 2007) but no other deep subhorizontal reflections are observed that could be interpreted as reflections from the Moho.

Fig. 4 shows the seismic image along orthogonal profile WG1 (Singh *et al.* 2008) with respect to the blow-up of the image along profile WG3 with a 3-D perspective. Although profile WG3 lies east of fracture zone F5, the crustal features are similar. A slight basement low at the SE end of the profile might be associated with fracture zone F4 (Fig. 2). As expected, the thickness of the sediments increases towards the trench from 2 to 3.5 s. Similar to profile WG3 there is a strong reflection at 1.4 s below the basement, which is interpreted as the Moho. Singh *et al.* (2008) have shown that this reflection can be imaged down to 40 km depth beneath the Sumatra fore arc basin. The oceanic part of profile WG2 lies in the complex zone between F6 and F7, and hence the reflection from the Moho is weaker, similar to profile WG3.

The extra-long streamer data (12 km) allowed us to determine the P -wave velocity in the sediments and crust accurately, particularly given the seafloor and sediments are nearly flat and therefore 1-D approximation used in analysis is valid (Fig. 5). The velocity in the turbiditic sediments varies from 1.8 to 3.3 km s^{-1} , lower than that suggested by Dean *et al.* (2010) who have used only a 2.4-km-long streamer (Fig. 5). The velocity in the pelagic sediment is $\sim 3.8 \text{ km s}^{-1}$. P -wave velocity between the basement and the Moho reflection varied from 6 to 6.5 km s^{-1} , which is consistent with the average crustal velocity of old oceanic crust (White *et al.* 1992). It should be noted that there is a moveout of about 850 ms for the Moho reflection at the farthest offset, and hence velocity in the crust is very well constrained, unlike that for short streamer data. However, we had no constraints on velocity in the mantle, and hence

we picked an arbitrary velocity of 8.1 km s^{-1} . There are dipping reflections in the mantle (Singh *et al.* 2007), but the 1-D velocity analysis is not valid for these events. The velocity along the whole profile is similar to that shown in Fig. 5.

5 REFRACTION DATA AND RESULTS

To study subduction zone processes, coincident refraction data were acquired along profiles WG1 and WG2. Ocean bottom seismometers (OBS) were placed every 4.6 and 8.1 km along profiles WG1 and WG2, respectively (Fig. 6). An array of 18 airguns with a total volume of 8260 cubic inch in a single bubble mode (Avedik *et al.* 1993) was fired at 150 m intervals. To determine the velocity at the end of seismic reflection line, 1–2 OBS were placed along the extended line and shots were fired for another 40 km along the extended line (Figs 2 and 6). The data quality is generally good (Fig. 7); one can clearly see the crustal and mantle arrivals from 10 to 60 km distance range. There are some arrivals that could be interpreted as wide-angle reflections from the oceanic Moho (PmP), but they are not as obvious as one generally observes PmP arrivals from oceanic Moho (Ranero & Sallares 2004), which could be due to the presence of thick sediments and thin crust. We have picked the first arrivals and performed tomographic inversion to determine the velocity structure of the crust and upper mantle.

First arrival traveltimes were made manually on the 51 and 48 OBSs along WG2 and WG1 profiles, respectively. The data were filtered to 5–25 Hz before picking. We picked $\sim 30\,000$ picks in total along each profile, and are used as input for tomographic inversion. For each data point, a picking uncertainty was assigned,

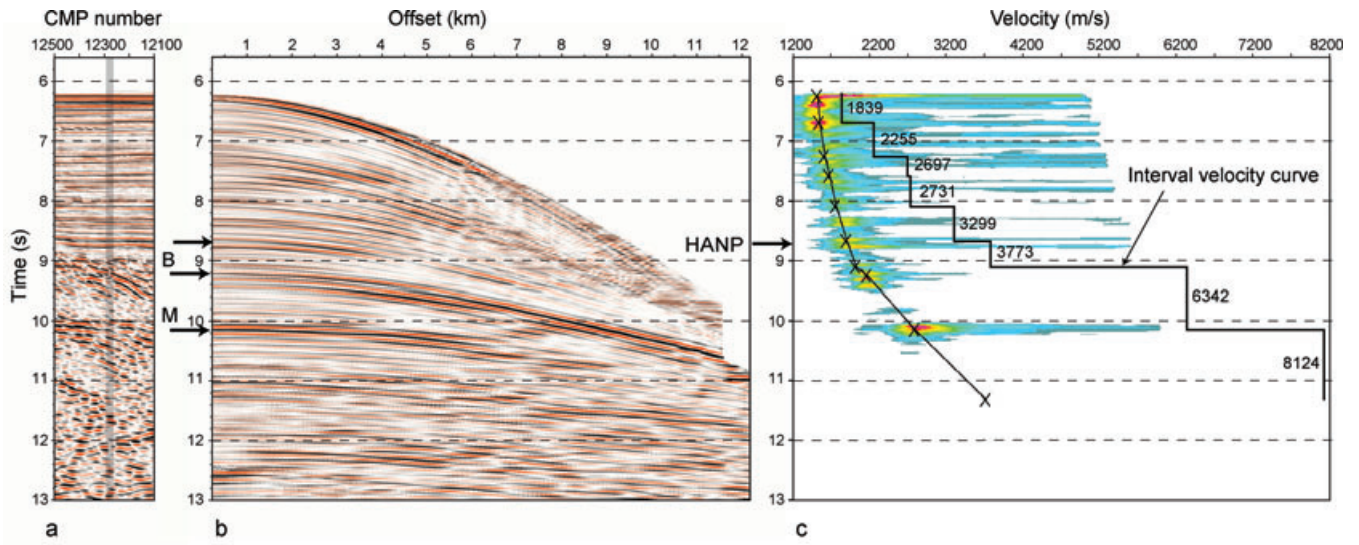


Figure 5. (a) Stacked section with the location of super-CMP (common mid-point) gather 12 284–12 303 on the migrated stack section as marked on Fig. 3. (b) Super-CMP gather 12 284–12 303 as a function of offset *versus* time. (c) Semblance panel (red-yellow-green-blue) with the associated root mean square and interval velocities superimposed. B, Basement; M, Moho; HANP, high amplitude negative polarity reflector.

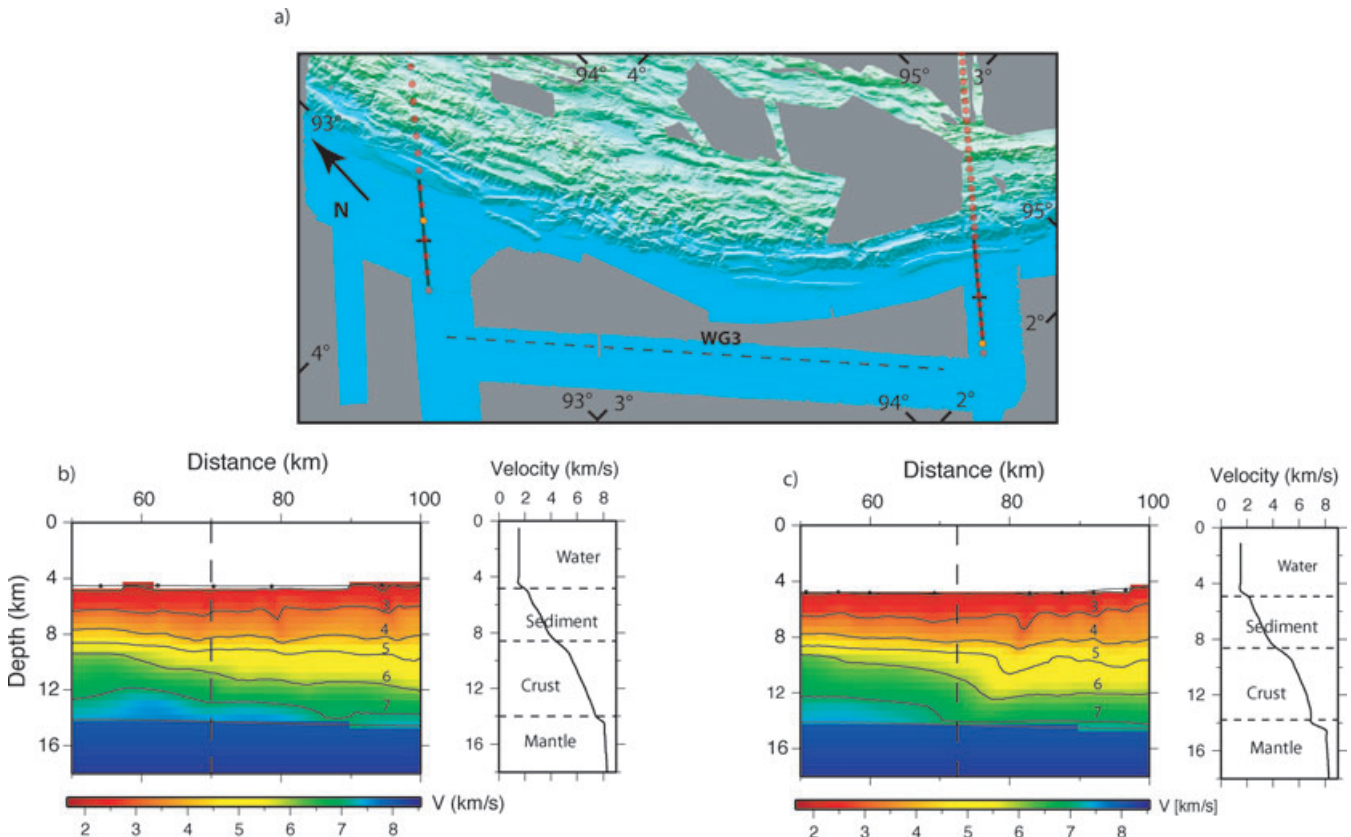


Figure 6. *P*-wave velocity determined using traveltimes tomography from ocean bottom seismometer (OBS) data along oceanic section of across-trench profiles at either end of profile WG3. (a) The locations of profiles WG1, WG2 and WG3. Red dots are the OBS locations, and orange dots are the data shown in Fig. 7. The black connecting lines indicate the location of two-dimensional velocity model (left) and crosses indicate one-dimensional velocity model (right) in Figs (b) and (c). The velocity in sediments varies from 1.7 to 4.5 km s⁻¹. There is a change in gradient at sediment–basalt interface. Because there is a thick sedimentary layer over the top of thin oceanic crust, the tomographic method provides only a smooth crustal velocity; the average crustal velocity is $\sim 6.2 \pm 0.4$ km s⁻¹. The velocity below the Moho is 8.0 ± 0.2 km s⁻¹. Thin black contours are *P*-wave velocities in km s⁻¹. The crustal thickness is 4.5 ± 0.5 km and 5.0 ± 0.5 km, consistent with reflection results along profiles WG1 and WG3, respectively.

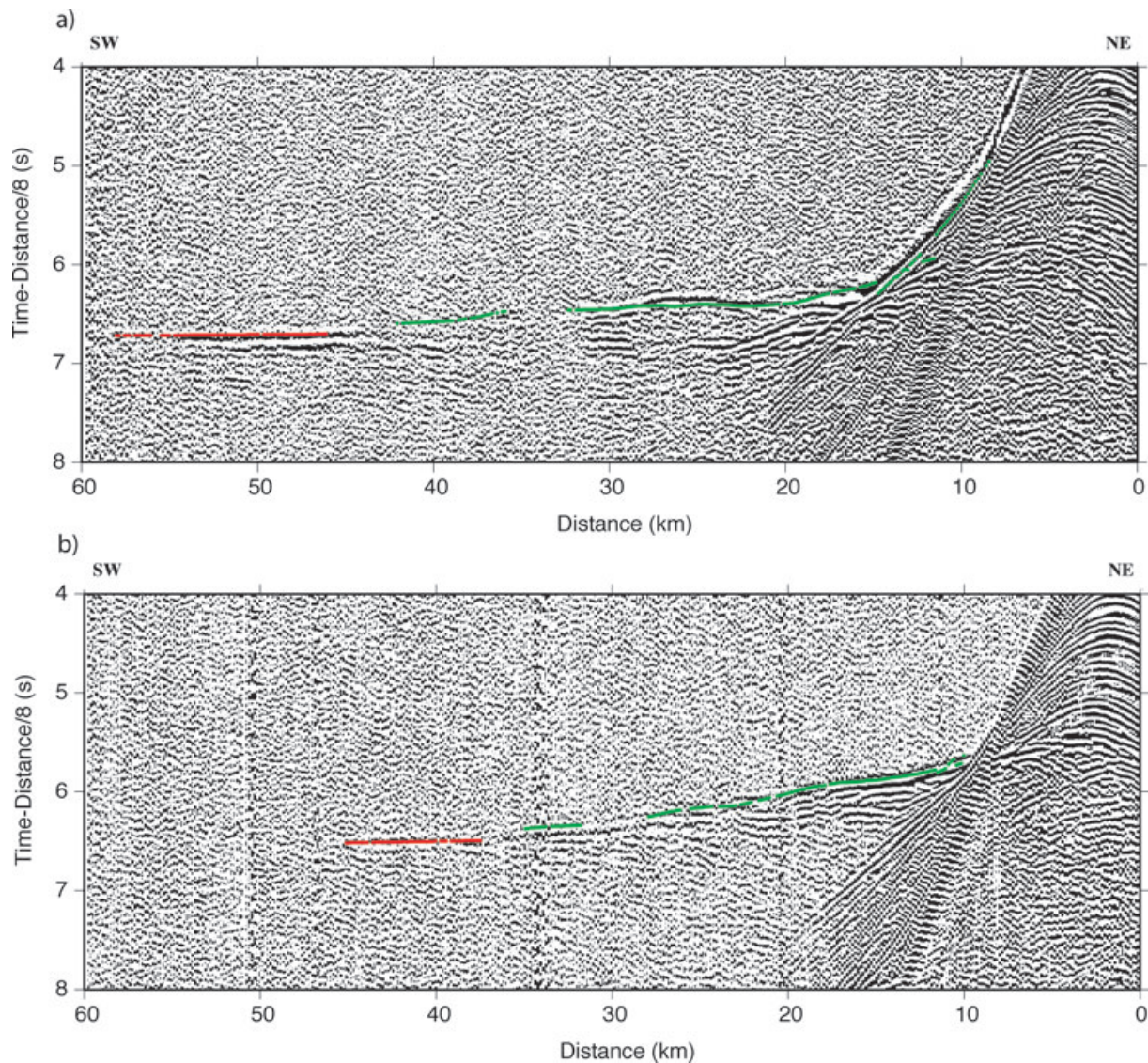


Figure 7. Most representative wide-angle seismic data along profile WG2 (a) and WG1 (b). OBS seismic gathers have been plotted at reduced velocity of 8 km s^{-1} . The picked arrival times (red) and those predicted from the inverted velocity model (blue) are plotted, the model fits the observed traveltime picks within picking uncertainty estimates.

which varied from 50 to 180 ms, from near to far offset. To obtain the tomographic image of the subsurface an adaptive traveltime inversion algorithm was implemented (Trinks *et al.* 2005) where the velocity cells were parameterized with an adaptive triangular gridding scheme. The starting value for the triangle side was 5 km, which was successively reduced to 2.5 and 1.25 km. A smoothing regularization was applied to obtain smooth velocity and to avoid over-fitting the data, which also varied for different triangle size. The starting model was a 1-D crustal velocity model. Several runs were made with decreasing triangle size and smoothing regularization. The result from the previous run was used as a starting model for the next run. The initial χ^2 value was 173, which reduced to 2.7 during the final run. The final root mean square residual was decreased to 132 ms. The OBS data provided the *P*-wave velocity model of the oceanic crust to depths of up to ~ 16 km.

Although a part of these profiles cut across fracture zones and some of the ray paths go through accretionary sediments, one can

get a good estimation of velocity of the oceanic crust and upper mantle. Because we have used a regularized tomography (Trinks *et al.* 2005), the velocity model is smooth, and boundary is not sharp. The velocity in the sediments is between 2 and 4 km s^{-1} , similar to seismic reflection results (Fig. 6). The velocity in the crust is between $4.0\text{--}4.5$ and 7 km s^{-1} and that in the mantle 7.5 km s^{-1} . There is a lateral variation in the crust, but the average crustal velocity along the oceanic part of these profiles is $6.2 \pm 0.4 \text{ km s}^{-1}$, leading to average crustal thicknesses of $4.5 \pm 0.5 \text{ km}$ along WG1 and $5.0 \pm 0.5 \text{ km}$ along WG2 (Fig. 6). The Pn arrivals (Fig. 6) require a mantle velocity of $7.8 \pm 0.3 \text{ km s}^{-1}$, suggesting that the prominent reflection is indeed crust–mantle boundary, Moho. Refraction-based crustal thicknesses along profiles WG1 and WG2 are slightly higher ($4.5\text{--}5 \text{ km}$) than that along profile WG3 ($3.5\text{--}4.5 \text{ km}$) but it is within the uncertainty in crustal thickness estimation using refraction method. Furthermore, profiles WG1 and WG2 lie on different segments. Our results are consistent with independently derived velocity by Dessa *et al.* (2009).

6 THIN CRUST

Our results suggest that the crust along profile WG3 is extremely thin (3.5–4.5 km), that is ~40 per cent thinner than normal oceanic crust. There is a gradual increase in thickness from 3.5 km in the southeast to 4.5 km in the northwest, which accompanies a change in crustal age from 55 to 58 Ma (Figs 1 and 2). The younger (52–54 Ma) crust east of the fracture zones F4/F5 is ~4.5 km thick (Fig. 4). At the northwestern end of the profile, the rough basement topography does not permit a clear imaging of the Moho reflection, but a discontinuous reflection is observed at ~5 km below the basement. The same strong, continuous reflector is also imaged on the dip line WG1 (Figs 2 and 4) where it could be followed for about 200 km down to 40 km depth beneath the overriding Sunda Plate (Singh *et al.* 2008). In the absence of more numerous direct crustal thickness measurements in the Wharton basin, the lateral extent of this crustal thickness anomaly is difficult to determine but our present data show that thin crust seems to be present beneath at least two major segments (300 km wide E–W zone) of the oceanic crust between fracture zones F3 and F7 (Fig. 2).

Moreover, residual basement depth can reflect anomalies in crustal thickness at intermediate wavelength (e.g. Loudon 2004). Fig. 8 shows a map of the residual basement depth anomalies in the Wharton basin, compared to the GDH1 depth-age model by Stein

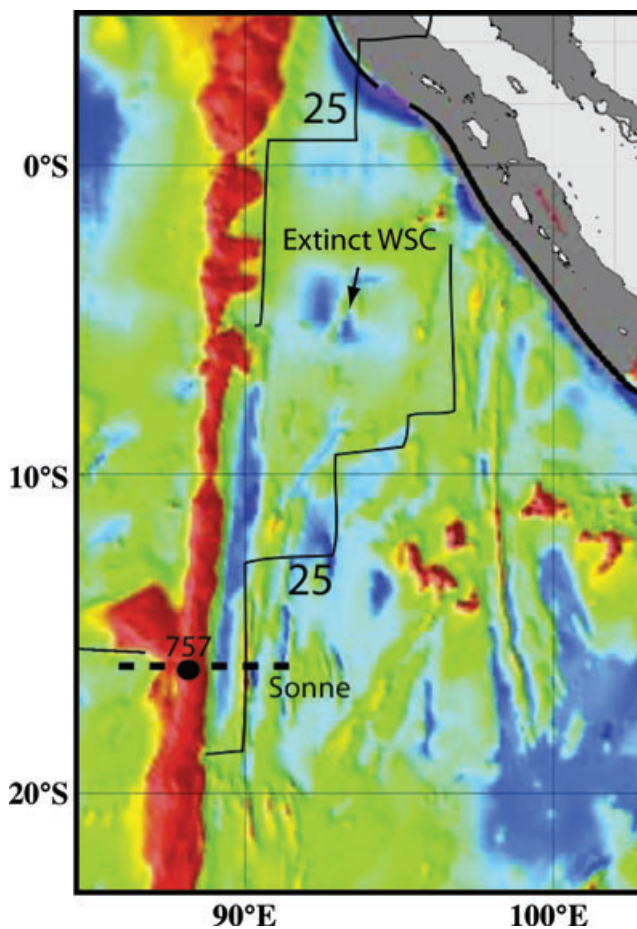


Figure 8. Residual basement depth computed by calculating the difference between the basement depth predicted by the GDH-1 model (Stein & Stein 1992) and the sediment unloaded basement depth. Modified from Fig. 11 of Müller *et al.* (2008). The magnetic anomaly 25 is marked, showing the position of WSC 56 Ma ago. Profile WG3 crosses anomaly 25–26 (Fig. 2).

& Stein (1992). This map is a close up of the global map by Müller *et al.* (2008) and was drawn with the data obtained from http://www.ngdc.noaa.gov/mgg/ocean_age/data/2008/grids/residual_basement/. Different depth-age models all lead to similar results in our area of interest (Müller *et al.* 2008). Interestingly enough, our zone of small crustal thickness corresponds to an abnormally low seafloor depth, and the conjugate isochron on the Australian flank of the Wharton basin shows an equivalent anomaly. It is therefore compatible with a similar crustal thinning. In the same spreading corridors, another low depth anomaly is localized on the extinct WCS, which probably reflects thinner crust due to starving of the ridge as the spreading centre became extinct. Between the extinct WCS and chron 25, the basement appears roughly normal. The basement appears shallower for the crust older than chron 26 on the Australian flank of the Wharton basin. At the latitude of ODP site 757, the seismic experiment Sonne (Fig. 8) has shown a normal crust thickness and even some underplating under the Wharton Basin (Grevemeyer *et al.* 2001).

Thin crust is generally associated with ultra-slow spreading ridges (Jokat & Schmidt-Aurch 2007) or fracture zones along slow spreading ridges (Detrick *et al.* 1993) but its presence at a fast spreading centre (~120 mm yr⁻¹) is very unusual. Relatively thin crust (~5 km) has also been reported near ODP Hole 504B (Collins *et al.* 1989), IODP Hole 1256 (Hallenborg *et al.* 2003), South American Trench (Grevemeyer *et al.* 2007) in the Pacific Ocean, and in the Arabian Sea (Collier *et al.* 2009), among other places but a crustal thickness of 3.5 km has never been observed before in a fast spreading ridge context. It could be caused by a very fast spreading effect, chemical or temperature anomalies in the mantle, or due to a combined effect.

Very fast spreading might lead to a situation where plates move apart faster than there is enough melt produced during decompressive melting in the mantle to form normal oceanic crust. However, there are no experimental data or theoretical model to support such a hypothesis. Furthermore, results from southern East Pacific Rise (ultra-fast spreading) show that the crust there is ~1.9 s (6 km) thick and is uniform (Kent *et al.* 1994; Canales *et al.* 1998; Grevemeyer *et al.* 1998), and therefore, one would require other explanations for the thin crustal observation.

Mantle compositional anomaly will cause variations of melt supply along mid-ocean ridges. More primitive mantle produces excessive melt because it contains more volatiles, particularly water, which cause the solidus to lie at greater depths (Asimow & Langmuir 2003) and because it is enriched in fusible elements. By contrast, mantle that has been depleted by an earlier episode of melting shall produce less melt as it rises up under the ridge. Collins *et al.* (1989) explained the existence of thin (5 km) crust near ODP Hole 504B by the presence of depleted mantle.

Higher temperature in the mantle caused by the presence of a plume would result in higher melt production and hence thicker crust (Klein & Langmuir 1987; White *et al.* 1992) whereas thin crust production would require lower than normal mantle temperature. Current mantle melting models indicate that to decrease crustal thickness by 1 km, one would require a decrease of ~15°C from the normal mantle temperature (Klein & Langmuir 1987; White *et al.* 1992). Therefore, to decrease the thickness by 2–3 km from the crustal thickness value of 6–7 km, or to decrease the melt production by ~40 per cent, one would require a decrease in mantle temperature of ~40–50 °C.

Mantle convection produces lateral temperature variations on a wide range of time and length scales, and low temperature anomalies are expected in domains of mantle downwellings (Christensen

& Harder 1991). However, there is no evidence for large expanses of thin crust in fast-spreading oceans. On the longest seismic line (6100 km) ever shot over the Pacific Plate covering 0- to 85-Ma-old crust formed at the fast spreading East Pacific Rise (Eittreim *et al.* 1994) the crustal thickness is 6–6.5 km, consistent with other seismic studies (White *et al.* 1992). Therefore, thin crust in fast spreading ridge environment cannot be explained by widespread small-scale convection due to lithospheric cooling (Parson & McKenzie 1978) or convection cells in the upper mantle (McKenzie *et al.* 1980).

7 PLUME–RIDGE INTERACTION

7.1 Plume–lithosphere interaction

As the short review above indicates, it is not easy to produce thin crust in a fast spreading ridge context. However, we have not yet used one important factor of the Indian ocean geodynamics: the proximity of the WSC to the Kerguelen hotspot and its track on the Indian Plate, the Ninety-East ridge. As has been proposed by Morgan (1971) and supported by a large number of theoretical, experimental and numerical studies in the last 40 years (see Ito *et al.* 2003 for recent reviews), a hot rising plume can have a significant effect on the lithosphere. Its best-known manifestations are volcanism, which leaves a track of seamounts on the moving overriding lithosphere, geochemical isotopic anomalies on the volcanoes, and the bathymetric swell supported by the upwelling hot material. For a strong plume on a fast moving plate, such as present-day Hawaii, the plume impact would produce an elongated puddle of flowing hot plume material that should extend to at least 30 Ma downstream from the plume (Fig. 9, Ribe & Christensen 1994, 1999). The velocity of the Indian Plate during the formation of the Ninety-East ridge was comparable to the Pacific Plate velocity today. No reliable estimate of the buoyancy flow of the Kerguelen plume at that time exists, but the magma output rates at that time ($\sim 0.1 \text{ km}^3 \text{ yr}^{-1}$, Coffin *et al.* 2002) was similar to current Hawaiian rates. This might suggest, as a first approximation, that the Kerguelen plume buoyancy flux was similar to Hawaii's today. In this case, the same type of

elongated hot puddle is expected to have formed. Underplating (Grevemeyer *et al.* 2001) and prolonged crustal growth inferred from the anomalous subsidence history of the Ninety-East Ridge (Grevemeyer & Flueh 2000) supports this view of flowing hot material from the Kerguelen hotspot along the volcanic track. This is also consistent with seismic evidence for extensive chemical modification of the lithospheric mantle along the portion of the Ninety-East ridge currently subducting under the Sumatra-Adaman arc. The anomalous seismic velocities imaged there are best explained by orthopyroxene-rich compositions, which would have formed by the interaction of upwelling magmas with pre-existing lithosphere.

So far, all this explain well the anomalously thick crust found along the 90°E ridge, but not the presence of anomalously thin crust close by. However, close examination of the laboratory and 3-D numerical models of plume–lithosphere interaction reveals the presence of a thin sheet of colder material along the edges of the hot plume puddle. This is clearly seen in the pioneering experimental work of Olson *et al.* (1988) where they studied the penetration of a hot plume through a cold strongly temperature-dependent viscosity lithosphere. More recent experiments (Androvandi 2009) using improved techniques of visualization of the temperature and velocity fields (Fig. 10) allowed us to quantify the phenomenon. 3-D numerical models focussing on the interaction of a steady plume stem under a fast moving lithosphere (e.g. Ribe & Christensen 1994, 1999) show that a thin cold sheet is also present along the elongated hot plume puddle (Fig. 9) with a temperature anomaly about 50°C lower than the mantle at the same depth in the asthenosphere. For the case of a ridge-centred plume stem, Ito *et al.* (1999) found a local minimum in both upwelling and crustal thickness occurring at the distal edge of the plume influence.

7.2 Origin of the cold downwelling

The cold curtain observed above is formed from lithospheric material coming from the bottom of the cold lithosphere. Because of the strongly temperature-dependent viscosity of the mantle, the viscosity of the cold thermal boundary layer (TBL) of the mantle (i.e. the lithosphere) increases from the asthenosphere to the surface.

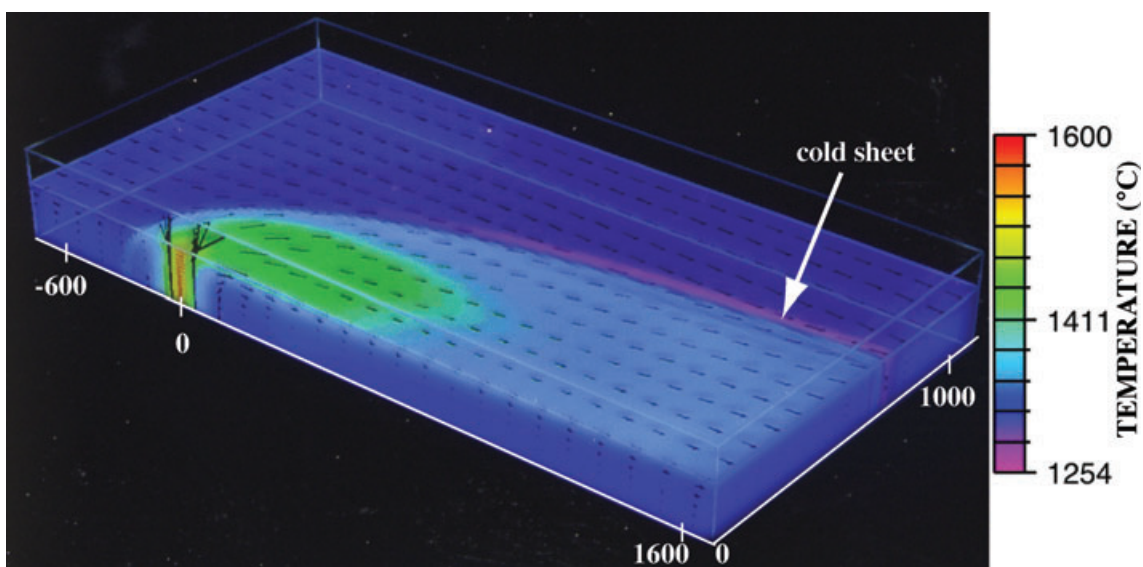


Figure 9. Temperature in degrees Celsius (colour) and velocity (arrows) fields for a plume with Newtonian temperature- and depth-dependent rheology. The model parameters were taken to fit the Hawaiian case (plate velocity = 8.6 cm yr^{-1} and Buoyancy flux = 4.1 Mg s^{-1}). The dimensions of the box are indicated in km. Only the left half (looking downstream) of the plume is shown, and the upper surface displayed is at 150 km. (Adapted from Ribe & Christensen 1994).

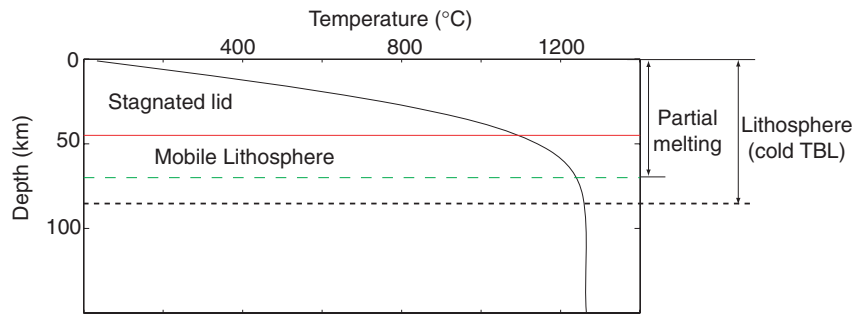


Figure 10. Thermal structure of a 18-Ma-old lithosphere: the temperature profile has been calculated from the conductive cooling of a half-space cooled from above (taking the heat diffusivity $\kappa = 8 \times 10^{-7} \text{ m}^2 \text{ s}^{-1}$). The thickness of the stagnant and mobile parts of the lithosphere is calculated using eq. (1).

Therefore flow, forced at the bottom of the lithosphere by an impinging plume, will be able to displace only the bottom less viscous part of the lithosphere. Because cold material is denser and hence gravitationally unstable, it should therefore generate local downwellings.

Theoretical, laboratory and numerical studies have shown that the portion of lithosphere that can be destabilized is such that the temperature difference across it is less than a critical temperature scale (Morris & Canright 1984; Davaille & Jaupart 1993; Solomatov & Moresi 2000),

$$\Delta T_c = 2.24 \times \eta(T_m) / (d\eta/dT(T_m)), \quad (1)$$

where T_m is the fluid temperature below the cold TBL and η is the temperature-dependent viscosity. These criteria predict well the occurrence of small-scale convection under the cold lithosphere. For mantle creep rheologies (either Newtonian diffusion creep or non-Newtonian dislocation creep), and a temperature difference of

1300 °C across the whole lithosphere, the temperature difference across the mobile layer will be between 50 and 200°C and the mobile layer would be 10–30 km thick (Fig. 10) (e.g. Davaille & Jaupart 1994; Solomatov & Moresi 2000; Huang *et al.* 2003; Korenaga & Jordan 2003).

The pioneering numerical study by Olson *et al.* (1988) suggests that impacts of plume heads under the lithosphere would give similar values. We recently re-examined this problem using laboratory experiments. We use sugar syrup as an analogue to mantle material because its viscosity depends strongly on temperature. The fluid was seeded with thermochromic liquid crystals (TLCs) and tiny hollow glass spheres. A given type of TLCs reflects light at a given temperature. So illuminated by a laser sheet, a mixture of TLCs will image several 'isotherms' as bright lines, and allow to follow the temperature field. Tracking the trajectories of the glass spheres will allow to determine the velocity field (see Davaille & Limare 2007 for a detailed description of the techniques) (Fig. 11). The layer

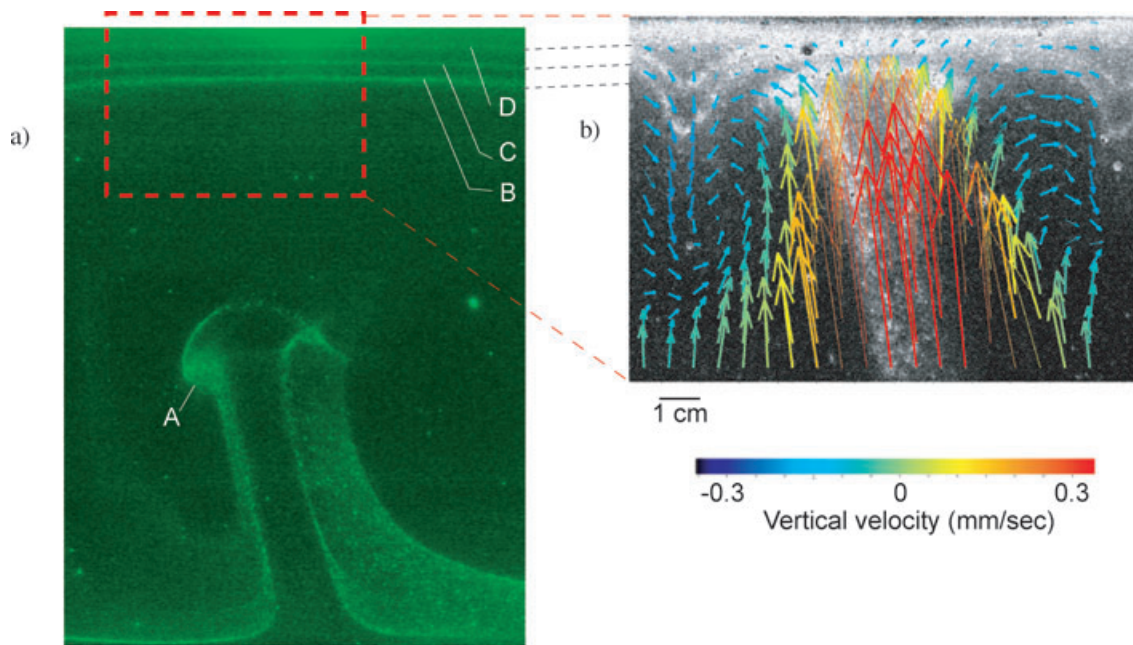


Figure 11. Experimental results: (a) A tank (30 × 30 cm; height 15 cm) of sugar syrup is cooled from above (at $T = -16 \text{ }^\circ\text{C}$) and heated from below (at $T = 52.4 \text{ }^\circ\text{C}$). The tank bulk interior is at temperature $T_m = 36 \text{ }^\circ\text{C}$. The viscosity ratio between the cold and the hot fluid is 3245, and the Rayleigh number, characterizing the intensity of convection, is 3.4×10^6 , within mantle convection range. Bright white lines are isotherms ($A = 40.5 \text{ }^\circ\text{C}$; $B = 31.4 \text{ }^\circ\text{C}$; $C = 24.6 \text{ }^\circ\text{C}$; $D = 10.4 \text{ }^\circ\text{C}$). A cold TBL below the upper surface is developing, while the bottom hot TBL has already become unstable and has generated a hot plume. The lateral dimension of the image is 10 cm. (b) Close up on the thermal (bright white lines) and velocity structures (coloured arrows) after the plume impact. The plume is surrounded by a ring of colder material and consequently the two bottom isotherms of the cold TBL (within the mobile part) are distorted.

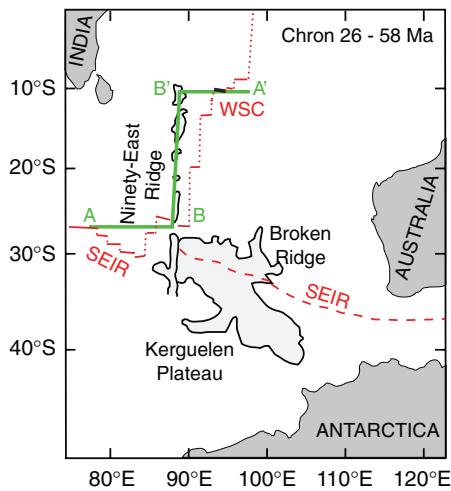


Figure 12. Reconstruction of the Indian Ocean at Chron 26 (58 Ma). The plate boundaries are indicated by red curves. The red solid segment represents the spreading axis along SEIR and WSC and black line indicates the segment of the Wharton spreading where the crust along profile WG3 was created. Discontinuities are marked by dotted lines. Dashed curve is the plate boundary between Australia and Antarctica. The Ninety-East ridge is generated by a hotspot located at B (adapted from Royer & Sandwell 1989). The green line (ABB'A') is the section of the diagram used in Fig. 13.

of fluid was cooled from above at a constant temperature so that a cold TBL developed at the top of the box (Fig. 11a). For the sugar syrup used in the laboratory, ΔT_c was $\sim 14.9^\circ\text{C}$. The tank was also heated from below, leading to the development of hot thermal plumes. Upon impinging under the cold boundary they displaced the bottom part of the cold TBL. We can see in Fig. 11(b) that the isotherms distorted by the incoming plume correspond to the zone where $T_m - \Delta T_c \leq T \leq T_m$. The hot plume puddle just below the lithosphere is therefore surrounded by a cold downwelling. Inspection of the velocity fields (Fig. 11b) shows that the associated downwelling motions are localized in the vicinity of the lithosphere (in other words, they do not reach the bottom of the experimental

box). Those results suggest that (1) upon impact, a hot mantle plume could displace the lower mobile part of the lithosphere towards its edge forming a colder downwelling sheet; and (2) eq. (1) can predict the magnitude of the cold temperature anomaly associated with it. Such a model predicts well the 50°C anomaly seen in the numerical model of Hawaii (Fig. 9). Moreover, because this displaced material is not only cold but consists of older lithosphere, it is likely to have gone through prior melting episodes and hence would be depleted.

7.3 Interaction between the Kerguelen plume and the Wharton spreading centre

Fig. 12 shows the reconstruction of Indian Ocean region 58 Ma ago, when the Kerguelen hot spot would have been at the triple junction of WSC and SEIR. The crust along profile WG3 was formed 55–58 Ma ago on the WSC, therefore located ~ 2000 km (~ 18 Ma) downstream from the Kerguelen hotspot close to the Ninety-East Ridge (Fig. 12). The thermal structure of the lithosphere at this age (Fig. 10) suggests that most of the lithospheric material should be above 70 km depth, and therefore it is likely to have already encountered an episode of melt extraction (McKenzie & Bickle 1988). The stagnant part of the 18-Ma lithosphere is 45 km thick, whereas the mobile part is 20 km thick, prone to delamination by the Kerguelen plume, resulting in a cold downwelling sheet (Fig. 13). The WG3 segment could therefore have formed on this cold depleted material, producing thinner crust (Fig. 13). The slight thickening of the crust towards west (plume) of the profile could be explained by our model (Fig. 13).

Similar phenomena might have occurred in the Pacific Ocean where the observed thin crusts might have been formed by the interaction between the Galapagos hotspot and the Costa Rica Rift (ODP Site 504B) and East Pacific Rise (IODP Site 1256), respectively. Canales *et al.* (2002) found that crustal thickness along the Galapagos Spreading Centre decreased from 8 km near the Galapagos hotspot to 5.5 km away from the hot spot. It is possible that this less than normal (6 km) crustal thickness could be due to the plume–ridge interaction. The results presented here should be applicable for other plume–ridge interaction, and requires further investigation.

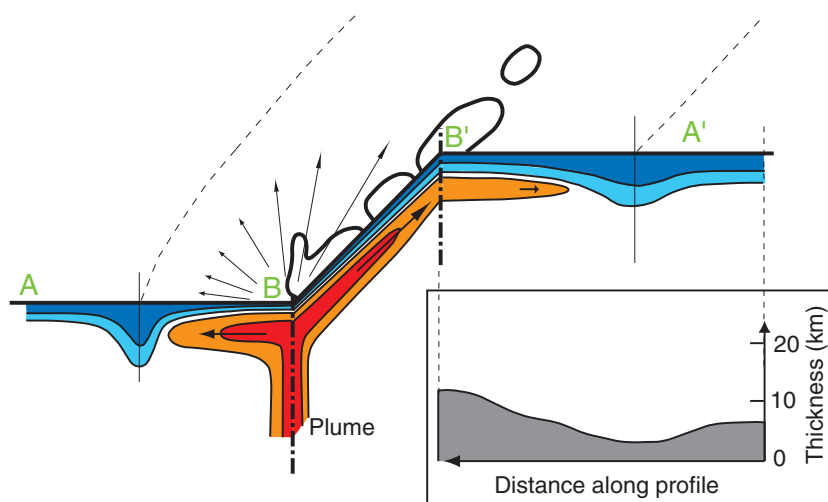


Figure 13. Three-dimensional sketch of the mantle flow along the profile A–B–B'–A' (green line in Fig. 12). The plume (in red and orange) impinges at B and spreads under the lithosphere. Because of plate motion, part of the plume flux is channelled along the track (as seen in Figs 9 and 11). The hot material is surrounded by a localized return flow of cold material (in blue). Point B' is 2000 km and 18 Ma downstream of point B. Insert: crustal thickness produced by the temperature structure along the profile B'–A' as if this profile was the WSC. Dashed line indicates the position of the cold channel on either side of the Ninety-East Ridge.

The thermal structure of mid-ocean ridges determines the depths and the nature (steady-state versus ephemeral) of magma lenses in the crust (Chen & Morgan 1996), responsible for forming the lower crust (gabbro). Because melt lenses are deeper for a colder axial regime (Chen & Morgan 1996) they should feed a thicker section of dikes, and therefore, the combined effect of thin crust and deeper melt lens should produce an anomalous gabbro-dike thickness ratio. A non-steady-state melt lens in the crust may lead to less frequent eruptions, resulting in a greater local variability of the composition of erupted basalt (Rubin & Sinton 2007) in a fast spreading environment.

8 CONCLUSIONS

Based on our study, we make the following conclusions:

1. The crust formed 55–58 Ma ago in the northern Wharton Basin is extremely thin (3.5–4.5 km).
2. A hot mantle plume impinging over a layer of cold lithosphere can produce a thick layer of cold lithosphere around it.
3. Thin crust in the northern Wharton Basin could have formed by the interaction between Kerguelen hotspot and Wharton Spreading Centre 55–58 Ma ago.

ACKNOWLEDGMENTS

We thank Schlumberger for its overall support and contribution to this project, and in particular, we recognize the efforts made by the captain and crew of the WesternGeco Q-Marine* (where asterisk (*) is the Mark of Schlumberger) vessel, *Geco Searcher*. Agence Nationale de Recherche (France) and IPG Paris funded the participation of scientists in the survey. This is a collaborative project between the Government of Indonesia (BPPT & LIPI), Schlumberger (WesternGeco), and the Institut de Physique du Globe (IPG) de Paris. This work benefited from discussions with Neil Ribe and Garrett Ito, and the comments Tim Minshull, Ingo Grevemeyer and anonymous reviewers. IPG Paris contribution number #3098.

REFERENCES

Abercrombie, R.E., Antolik, M. & Ekstrom, G., 2003. The June 2000 Mw 7.9 earthquakes south of Sumatra: deformation in the India-Australia Plate, *J. geophys. Res.*, **108**, 2018, doi:10.1029/2001JB000674.

Androvandi, S., 2009. Convection multi-échelles dans un Manteau dont la viscosité dépend de la température, *PhD thesis*. Institut de Physique du Globe de Paris, France.

Asimow, P.D. & Langmuir, C., 2003. The importance of water to oceanic mantle melting regimes, *Nature*, **421**, 815–820.

Avedik, F., Renard, V., Allenou, J.P. & Morvan, 1993. “Single bubble” air-gun array for deep exploration, *Geophysics*, **58**, 366–382.

Barclay, A.H., Toomey, D.R. & Solomon, S.C., 1998. Seismic structure and crustal magmatism at the Mid-Atlantic Ridge, 35°N, *J. geophys. Res.* **103**, 17 827–17 844.

Barth, G.A. & Mutter, J.C., 1996. Variability in oceanic crustal thickness and structure: multichannel seismic reflection results from the northern East Pacific Rise, *J. geophys. Res.*, **101**, 17 951–17 976.

Bown, J.W. & White, R.S., 1994. Variation with spreading rate of oceanic crustal thickness and geochemistry, *Earth planet. Sci. Lett.*, **121**, 435–449.

Canales, J.P., Detrick, R.S., Bazin, S., Harding, A.J. & Orcutt, J.A., 1998. Off-axis crustal thickness across and along the East Pacific Rise within the MELT area, *Science*, **280**, 1218–1221.

Canales, J.P., Ito, G., Detrick, R.S. & Sinton, J., 2002. Crustal thickness along the western Galapagos Spreading Centre and the compensation of the Galapagos hotspot swell, *Earth planet. Sci. Lett.* **203**, 311–327.

Chauhan, A. *et al.*, 2009. Seismic imaging of forearc backthrusts at northern Sumatra subduction zone, *Geophys. J. Int.*, **179**, 1772–1780.

Chen, Y.J. & Morgan, J.P., 1996. The effects of spreading rate, the magma budget, and the geometry of magma emplacement on the axial heat flux at mid-ocean ridges, *J. geophys. Res.* **101**, 11 475–11 482.

Chen, Y., 1992. Oceanic crustal thickness versus spreading rate, *Geophys. Res. Lett.*, **19**, 753–756.

Christensen, U.R. & Harder, H., 1991. 3-D convection with variable viscosity, *Geophys. J. Int.*, **104**, 213–226.

Coffin, M.F., Pringle, M.S., Duncan, R.A., Gladchenko, T.P., Storey, M., Muller, R.D. & Gahagan, L.A., 2002. Kerguelen hotspot magma output since 130 Ma, *J. Petrol.*, **43**, 1121–1139.

Collins, J.A., Purdy, G.M. & Brocher, T.M., 1989. Seismic velocity structure at Deep Sea Drilling Site 504B, Panama Basin: evidence for thin oceanic crust, *J. geophys. Res.*, **94**, 9283–9302.

Collier, J.S., Minshull, T.A., Hammond, J., Whitmarsh, R.B., Kendall, J.M., Sansom, V., Lane, C. & Rumpker, G., 2009. Factors influencing magmatism during continental breakup: new insights from a wide-angle seismic experiment across the conjugate Seychelles-Indian margins, *J. geophys. Res.*, **114**, B03101, doi:10.1029/2008JB005898.

Davaille, A. & Jaupart, C., 1993. Transient high-Rayleigh number thermal convection with large viscosity variations, *J. Fluid Mech.*, **253**, 141–166.

Davaille, A. & Jaupart, C., 1994. Onset of thermal convection in fluids with temperature-dependent viscosity: Application to the oceanic mantle, *J. geophys. Res.*, **99**, 19 853–19 866.

Davaille, A. & Limare, A., 2007. Laboratory studies of mantle convection, in *Treatise of Geophysics*, Vol.7, pp. 89–165, eds Bercovici, D. & Schubert, G., Elsevier, Amsterdam.

Dean, S.M. *et al.*, 2010. Contrasting decollement and prism properties over the Sumatra 2004–2005 earthquake rupture boundary, *Science*, **329**, 207–210.

Deplus, C. *et al.*, 1998. Direct evidence of active deformation in the eastern Indian oceanic plate, *Geology*, **26**, 131–134.

Dessa, J.X., Klingelhoefer, G., Andre, C., Permana, H., Gutscher, M.A., Chauhan, A., Singh, S.C.; and the SUMATRA-OBS Scientific Team, 2009. Megathrust earthquakes can nucleate in the forearc mantle: evidence from the 2004 Sumatra event, *Geology* **37**, 659–662.

Detrick, R.S., Buhl, P., Vera, E., Mutter, J., Orcutt, J., Madsen, J. & Brocher, T., 1987. Multi-channel seismic imaging of a crustal magma chamber along the East Pacific Rise, *Nature*, **326**, 35–41.

Detrick, R.S., White, R.S. & Purdy, G.M., 1993. Crustal structure of North Atlantic fracture zones, *Rev. Geophys.*, **31**, 439–458.

Eittreim, S.L., Gnibidenko, H., Hellsley, C.E., Sliter, R., Mann, D. & Ragozin, N., 1994. Oceanic crustal thickness and seismic character along a central Pacific transect, *J. geophys. Res.*, **99**, 3139–3145.

Engdahl, E.R., Villasenor, A., DeShon, H.R. & Thurber, C.H., 2007. Tele-seismic relocation and assessment of seismicity (1918–2005) in the region of the 2004 Mw 9.0 Sumatra-Andaman and the 2005 Mw 8.6 Nias Island Great earthquakes, *Bull. seism. Soc. Am.*, **97**, S1–S19.

Frey, F.A., Coffin, M.F., Wallace, P.J. & Weis, D., 2003. Leg 183 synthesis: Kerguelen Plateau–Broken Ridge—a large igneous province, in *Proceedings of the ODP, Science Results*, pp. 1–48, eds Frey, F.A., Coffin, M.F., Wallace, P.J. & Quilty, P.G., Ocean Drilling Program, College Station, TX.

Fullerton L.G., Sager W.W. & Handschumacher D.W., 1989. Late Jurassic—early Cretaceous evolution of the eastern Indian Ocean adjacent to north-west Australia, *J. geophys. Res.*, **94**, 2937–2953.

Gaina, C., Muller, R.D., Brown, B., Ishihara, T. & Ivanov, S., 2007. Breakup and early seafloor spreading between India and Antarctica, *Geophys. J. Int.*, **170**, 151–169.

Graindorge, *et al.*, 2008. Impact of lower plate structure on the upper plate deformation at the NW Sumatra convergent margin from seafloor morphology, *Earth planet. Sci. Lett.*, **275**, 201–210.

Grevemeyer, I. & Flueh, E.R., 2000. Crustal underplating and its implications subsidence and state of isostasy along the Ninetyeast Ridge hotspot trail, *Geophys. J. Int.*, **142**, 643–649.

Grevemeyer, I., Flueh, E.R., Reichert, C., Bialas, J., Klaschen, D. & Kopp, C., 2001. Crustal architecture and deep structure of the Ninetyeast Ridge

- hotspot trail from active-source ocean bottom seismology, *Geophys. J. Int.*, **144**, 414–431.
- Grevenmeyer, I., Ranero, C.R., Flueh, E.R., Klaschen, D. & Bialas, J., 2007. Passive and active seismological study of bending-related faulting and mantle serpentinisation at the Middle American trench, *Earth planet. Sci. Lett.*, **258**, 528–542.
- Grevenmeyer, I., Weigel, W. & Jennrich, 1998. C. Structure and ageing of oceanic crust at 14 degrees S on the East Pacific Rise, *Geophys. J. Int.*, **135**, 573–584.
- Hallenborg, E., Harding, A.J. & Kent, G.M., 2003. Seismic structure of 15 Ma oceanic crust formed at an ultra-fast spreading East Pacific Rise: evidence for kilometer-scale fracturing from dipping reflectors, *J. geophys. Res.*, **108**(B11), 2532, doi:10.1029/2003JB002400.
- Huang, J., Zhong, S.J. & van Hunen, J., 2003. Controls on sublithospheric small-scale convection, *J. geophys. Res.*, **108**, 2405, doi:10.1029/2003JB002456.
- Ito, G., Shen, Y., Hirth, G. & Wolfe, C.J., 1999. Mantle flow, melting, and dehydration of the Iceland plume, *Earth planet. Sci. Lett.*, **165**, 81–96.
- Ito, G., Lin, J. & Graham, D., 2003. Observational and theoretical studies of the dynamics of mantle plume-mid-ocean ridge interaction, *Rev. Geophys.*, **41**(4), 1017, doi:10.1029/2002RG000117.
- Jokat, W. & Schmidt-Aursch, M.C., 2007. Geophysical characteristics of the ultra-slow spreading Gakkel Ridge, Arctic Ocean, *Geophys. J. Int.*, **168**, 983–998.
- Kent, G.M., Harding, A.J., Orcutt, A.A., Detrick, R.S., Mutter, J.C. & Buhl, P., 1994. Uniform accretion of oceanic crust south of the Garrett transform at 14 15 S on the East Pacific Rise, *J. geophys. Res.*, **99**, 9097–9116.
- Klein, E.M. & Langmuir, C.H., 1987. Global relations of ocean ridge basalt chemistry with axial depth and crustal thickness, *J. geophys. Res.*, **92**, 8089–8115.
- Korenaga, J. & Jordan, T.H., 2003. Physics of multiscale convection in Earth's mantle: onset of the sublithospheric convection, *J. geophys. Res.*, **108**, doi:10.1029/2002JB001760.
- Liu, C.S., Curray, J.R. & McDonald, J.M., 1983. New constraints on the tectonic evolution of the eastern Indian Ocean, *Earth planet. Sci. Lett.*, **65**, 331–342.
- Louden, K.E., Tucholke B.E., & Oakey G.N., 2004. Regional anomalies of sediment thickness, basement depth and isostatic crustal thickness in the North Atlantic Ocean, *Earth planet. Sci. Lett.* **224**, 193–211.
- Martin, J., Ozbeck, A., Combee, L., Lunde, N., Bittleston, S., & Kragh, E., 2000. Acquisition of marine point receiver with a towed streamer, *Society of Exploration Geophysicists Extended Abstract ACQ 3.3*.
- McKenzie, D. & Bickle, M., 1988. The volume and composition of melt generated by extension of the lithosphere, *J. Petrol.* **9**, 625–679.
- McKenzie, D., Watts, A.B., Parsons, B. & Roufousse, M., 1980. Platform of the mantle convection beneath the Pacific Ocean, *Nature*, **288**, 442–446.
- Morgan, W.J., 1971. Convection plumes in lower mantle, *Nature*, **230**, 42–43.
- Morris S. & Canright, D.R., 1984. A boundary-layer analysis of Benard convection with strongly temperature-dependent viscosity, *Phys. Earth planet. Inter.*, **36**, 355–373.
- Muller, M.R., Minshull, T.A. & White, R.S., 2000. Crustal structure of the Southwest Indian Ridge at the Atlantis II Fracture Zone, *J. geophys. Res.*, **105**, 25809–25829.
- Müller, R.D., Sdrolias, M., Gaina, C. & Roest, W. R., 2008. Age, spreading rates, and spreading asymmetry of the world's ocean crust, *Geochem. Geophys. Geosyst.*, **9**, Q04006, doi:10.1029/2007GC001743.
- Olson, P., Schubert, G., Anderson, C. & Goldman, P., 1988. Plume formation and lithosphere erosion: a comparison of laboratory and numerical experiments, *J. geophys. Res.*, **93**, 15 065–15 084.
- Parkin, C.J. & White, R.S., 2008. Influence of the Iceland mantle plume on the oceanic crustal generation in the North Atlantic, *Geophys. J. Int.*, **173**, 168–188.
- Parsons, B. & McKenzie, D.P., 1978. Mantle convection and the thermal structure of the plates, *J. geophys. Res.*, **82**, 4485–4495.
- Patriat, P. & Achache, J., 1984. India-Eurasia collision chronology has implications for crustal shortening and driving mechanism of plates, *Nature*, **311**, 615–621.
- Ranero, C.R. & Sallarès, V., 2004. Geophysical evidence for hydration of the crust and mantle of the Nazca plate during bending at the north Chile trench, *Geology*, **32**, 549–552.
- Ranero, C.R., Reston, T.J., Belykh, I. & Gribidenko, H., 1997. Reflective oceanic crust formed at a fast spreading centre in the Pacific, *Geology*, **25**, 499–502.
- Reid, I. & Jackson, H.R., 1981. Oceanic spreading rate and crustal thickness, *Mar. geophys. Res.*, **5**, 165–172.
- Ribe, N.M. & Christensen, U.R., 1994. Three-dimensional modelling of plume-lithosphere interaction, *J. geophys. Res.*, **99**, 669–682.
- Ribe, N. & Christensen, U.R., 1999. The dynamic origin of Hawaiian volcanism, *Earth planet. Sci. Lett.*, **171**, 517–531.
- Royer, J.-Y. & Sandwell, D.T., 1989. Evolution of the eastern Indian Ocean since Late Cretaceous: constraints from Geosat altimetry, *J. geophys. Res.*, **94**, 13 755–13 782.
- Rubin, K.H. & Sinton, J. M., 2007. Inferences on mid-ocean ridge thermal and magmatic structure from MORB compositions, *Earth planet. Sci. Lett.*, **260**, 257–276.
- Slater, J.G. & Fisher, R.L., 1974. Evolution of the east-central Indian Ocean, with emphasis on the tectonic setting of the Ninetyeast Ridge, *Geol. Soc. Am. Bull.*, **85**, 683–702.
- Singh, S.C., Kent, G.M., Collier, J.S., Harding, A.J. & Orcutt, J.A., 1998. Melt to mush variations in crustal magma properties along the ridge crest at the southern East Pacific Rise, *Nature*, **394**, 874–878.
- Singh, S.C. et al., 2006. Seismic reflection images of the Moho underlying melt sills at the East Pacific Rise, *Nature*, **442**, 287–290.
- Singh, S.C. et al., 2007. Seismic reflection images of deep lithospheric faults and thin crust at the actively deforming Indo-Australian plate boundary in the Indian Ocean, *EOS, Trans. Am. geophys. Un.*, **88**, Fall Meet. Suppl., Abstract T22E-06.
- Singh, S.C. et al., 2008. Seismic evidence for broken oceanic crust in the 2004 Sumatra earthquake epicentral region, *Nat. Geosci.*, **1**, 771–781.
- Solomatov, V.S. & Moresi, L.N., 2000. Scaling of time-dependent stagnant lid convection: application to small-scale convection on Earth and other terrestrial planets, *J. geophys. Res.*, **105**, 21 785–21 817.
- Stein, C.A. & Stein, S., 1992. A model for the global variations in oceanic depth and heat flow with lithospheric age, *Nature*, **359**, 123–129.
- Tikku, A.A. & Cande, S.C., 1999. The oldest magnetic anomalies in the Australian-Antarctic Basin: are they isochrons? *J. geophys. Res.*, **104**, 661–677.
- Trinks, I., Singh, S.C., Chapman, C., Barton, P.J. & Bosch, M., 2005. Adaptive travel time tomography of densely sampled seismic data, *Geophys. J. Int.*, **160**, 925–938.
- Van Avendonk, H.J.A., Harding, A.J., Orcutt, J.A. & McClain, J.S., 2001. Contrast in crustal structure across the Clipperton transform fault from travel time tomography, *J. geophys. Res.*, **106**, 10 961–10 981.
- White, R.S., McKenzie, D. & O'Nions, R.K., 1992. Oceanic crustal thickness from seismic measurements and rare earth element inversions, *J. geophys. Res.*, **97**, 19 683–19 715.